ADVANCED FUNCTIONAL MATERIALS
www.afm-journal.de

Li-Doping and Ag-Alloying Interplay Shows the Pathway for Kesterite Solar Cells with Efficiency Over 14%

*Yuancai Gong, Alex Jimenez-Arguijo, Axel Gon Medaille, Simon Moser, Arindam Basak, Romain Scaffidi, Romain Carron, Denis Flandre, Bart Vermang, Sergio Giraldo, Hao Xin, Alejandro Perez-Rodriguez, and Edgardo Saucedo**

Kesterite photovoltaic technologies are critical for the deployment of light-harvesting devices in buildings and products, enabling energy sustainable buildings, and households. The recent improvements in kesterite power conversion efficiencies have focused on improving solution-based precursors by improving the material phase purity, grain quality, and grain boundaries with many extrinsic doping and alloying agents (Ag, Cd, Ge...). The reported progress for solution-based precursors has been achieved due to a grain growth in more electronically intrinsic conditions. However, the kesterite device performance is dependent on the majority carrier density and sub-optimal carrier concentrations of 10^{14}–10^{15} cm^{-3} have been consistently reported. Increasing the majority carrier density by one order of magnitude would increase the efficiency ceiling of kesterite solar cells, making the 20% target much more realistic. In this work, $LiClO_4$ is introduced as a highly soluble and highly thermally stable Li precursor salt which leads to optimal ($>10^{16}$ cm^{-3}) carrier concentration without a significant impact in other relevant optoelectronic properties. The findings presented in this work demonstrate that the interplay between Li-doping and Ag-alloying enables a reproducible and statistically significant improvement in the device performance leading to efficiencies up to 14.1%.

1. Introduction

The integration of photovoltaic (PV) technology in buildings and products (BIPV, PIPV) for self-sustainable architecture and Internet of Things (IoT) applications is pivotal to make the future society sustainable. The perspectives on the potential candidates for light-harvesting in in-situ energy consumption devices have drastically changed due to the progress of emerging thin-film kesterite ($Cu_2ZnSn(S,Se)_4$, CZTSSe) technology.[1,2] Based on earth-abundant and low-toxicity elements, kesterite absorber materials have experienced a drastic increase of certified efficiencies from 12.6% to almost 15% in only one year after one decade of performance stagnation.[2–4] This progress has been achieved with incremental progress after a breakthrough in the synthesis method using molecular inks, combined with selective doping/alloying strategies and heterojunction defect mitigation.[4–8] A controlled phase purity can be achieved by preparing

Y. Gong, A. Jimenez-Arguijo, A. G. Medaille, S. Giraldo, E. Saucedo
Electronic Engineering Department
Universitat Politècnica de Catalunya (UPC)
Photovoltaic Lab—Micro and Nano Technologies Group (MNT)
EEBE
Av Eduard Maristany 10–14, Barcelona 08019, Spain
E-mail: Edgardo.saucedo@upc.edu

Y. Gong, A. Jimenez-Arguijo, A. G. Medaille, E. Saucedo
Barcelona Center for Multiscale Science & Engineering
Universitat Politècnica de Catalunya (UPC)
Av Eduard Maristany 10–14, Barcelona, Catalonia 08019, Spain

A. Jimenez-Arguijo, A. G. Medaille, A. Perez-Rodriguez
Solar Energy Materials and Systems Group
Catalonia Institute for Energy Research (IREC)
Jardins de les Dones de Negre 1
Sant Adrià de Besòs, Barcelona 08930, Spain

The ORCID identification number(s) for the author(s) of this article can be found under https://doi.org/10.1002/adfm.202404669

DOI: 10.1002/adfm.202404669

S. Moser, R. Carron
Laboratory for Thin Films and Photovoltaics
Empa—Swiss Federal Laboratories for Materials Science and Technology
Überlandstrasse 129, Dübendorf 8600, Switzerland

A. Basak
Thin Film Photovoltaic Lab
School of Electronics Engineering
KIIT- Deemed to be University
Bhubaneswar, Odisha 751024, India

R. Scaffidi, B. Vermang
IMO
Hasselt University
Wetenschapspark 1, Diepenbeek 3590, Belgium

R. Scaffidi, B. Vermang
IMOMEC
IMEC
Wetenschapspark 1, Diepenbeek 3590, Belgium

R. Scaffidi, B. Vermang
EnergyVille 2
Thor Park 8320, Genk 3600, Belgium

amorphous kesterite phase precursors from designed molecular inks, enabling the precise control of phase evolution during the selenization step, thus resulting in high-quality grain.[5,6,8–10] The detrimental effects of lattice disorder (electrostatic potential fluctuations and lower defect formation energies) can be palliated by the implementation of isovalent (co)-alloying (Ag, Cd, and Ge).[7,11–13] Furthermore, significant progress in the chemical passivation of grain boundaries with non-isovalent (co-)doping (Ga) has also been achieved.[14]

Besides the mentioned strategies, majority carrier concentrations are crucial for the PV performance of the device. However, even though the optimal hole concentration for kesterite solar cell performance has been demonstrated to be 10^{16} cm^{-3}, consistently reported values for high-efficiency devices have remained within the range of only 10^{14}–10^{15} cm^{-3}.[4,8,15] The lack of significant progress by precise control of the hole density in molecular ink-based kesterite probably has its origin in an improved grain quality of the material and therefore a less defective and more electronically intrinsic and ordered kesterite phase.[16] The hole concentration in kesterite is governed by the presence of abundant I_{II} (Cu_{Zn}), II_I (Zn_{Cu}) and V_I (V_{Cu}) intrinsic defects.[17] The Cu_{Zn} presents a relatively high ionization energy, and V_{Cu} presents a relatively high formation energy even in the typical and optimal composition of Cu-poor and Zn-rich conditions. The partial substitution of Cu by Ag leads to a lower concentration of Cu_{Zn} due to the lower Cu chemical potential. The high formation energy of Ag_{Zn} leads to Ag atoms mostly incorporated in Cu positions, leading to a reduction of the hole density.[7,18] Also, the well-known formation of secondary phases prevents the regulation of the hole concentration through compositional optimization.[17] Therefore, Cu isovalent extrinsic doping and alloying agents (I = Li, Na, K, Rb, Cs, and Ag) are the most suitable potential candidates, which have demonstrated the potential to tune the hole concentration.[19–22] In contrast with heavier elements, Li has demonstrated higher solubility in kesterite as well as a shallow donor state Li_{Zn} with lesser ionization energy than Cu_{Zn} and lower formation energies than V_{Cu}.[23] Hence, the high potential of Li doping in kesterite materials has been previously identified, showing a remarkable increase in hole concentration and efficiency for Ag-free and low baseline performance devices.[21,23–27] Similarly, a beneficial interaction between Ag and Li soft post-deposition treatments (PDT) has been previously reported.[28,29]

However, previous works demonstrate that the implementation of Ag-alloying during grain growth is critical to improving the solar cell performance due to improvements in the morphology and cation (Cu—Zn) disorder, consequently, the hole density is reduced.[7,30] Similarly, the addition of Li precursor in the Ag-free kesterite solution can also improve the solar cell performance relating to improvements in the morphology and crystalline quality and, in contrast with Ag, a slight increase in the hole density is measured.[26] This work aims to demonstrate the possibility of specifically tailoring the material optoelectronic properties with Ag and Li multinary and isovalent doping and alloying. The incorporation of Li in the Ag-alloyed CZTSSe is achieved via the introduction of the $LiClO_4$ into the molecular ink, which is highly soluble in organic solvents to make the doping level more flexible. The beneficial effects of Ag alloying in morphology, crystalline quality, and disorder are preserved. Due to the high decomposition temperature of $LiClO_4$, it effectively delays the formation of Li_2Se. Consequently, a post-deposition treatment like (PDT-like) passivation and controlled doping for kesterite in high-temperature selenization processes can be achieved. The reduced occupancy of the Zn sites caused by Ag alloying enables a higher density of shallow acceptor Li_{Zn} defects leading to a remarkable increase in the hole concentration of one order of magnitude. Through this synergy with Ag, the introduction of 2% $LiClO_4$ in the precursor ink leads to an absorber material with high crystalline quality, low disorder, and optimal hole concentration for photovoltaic performance enabling a maximum efficiency of 14.1%.

2. Results and Discussion

The previous report demonstrated a significant exchange between Na and Li during the high-temperature selenization process,[31] complicating the understanding of the true role of Li in kesterite. To mitigate uncertainties and comprehend the specific impact of Li on kesterite, we introduced SiO_x as a Na diffusion barrier at the bottom of the Mo layer. The device architecture is depicted in **Figure 1a** and comprises Soda-lime glass (SLG)/SiO_x/Kesterite/CdS/i-ZnO/ITO. With this, the out-diffusion of alkali metals from the SLG can be avoided, however, the exchange of Li and Na through the gaseous Na—Se and Li—Se phases cannot be supressed. The introduction of different $LiClO_4$ concentrations from 0.015 to 0.78 M, corresponding to ratios of Li/(Cu+Ag) of 2–100% have been explored. In this work, the effects of the addition of $LiClO_4$ in the solution are investigated by keeping the Cu and Ag concentration constant, implying that the cation ratio [I]/[II]+[IV] is increased from 0.75 to 1.5, depending on the Li concentration. The addition of $LiClO_4$ in the precursor solution leads to significant changes in the solar cell device performance, as showcased in Figure 1b–e,f.

The samples with Li concentration in the range of 2% to 10% show a remarkable increase in the open-circuit voltage (V_{OC}) and fill factor (FF), demonstrating a flexible optimal range of Li incorporation. Specifically, the sample with 2% Li/(Cu+Ag) content shows an impressive increase of FF, improving the reference by almost 10% in absolute value. The slight dispersion of the low Li content devices is an indication of the homogeneity of the beneficial effects induced by the introduction of Li, leading to a significant improvement in the average value of the power conversion efficiency (PCE) from 9.8% to 11.4%. In contrast, the samples

R. Scaffidi, D. Flandre
ICTEAM
Université Catholique de Louvain
Place du Levant L5.03.02, Louvain-la-Neuve 1348, Belgium
H. Xin
State Key Laboratory for Organic Electronics and Information Displays
College of Chemistry and Life Sciences
Nanjing University of Posts & Telecommunications
Nanjing 210023, China
A. Perez-Rodriguez
IN2UB
Departament d'Enginyeria Electrònica i Biomèdica
Universitat de Barcelona
Carrer de Martí i Franquès 1, Barcelona 08028, Spain

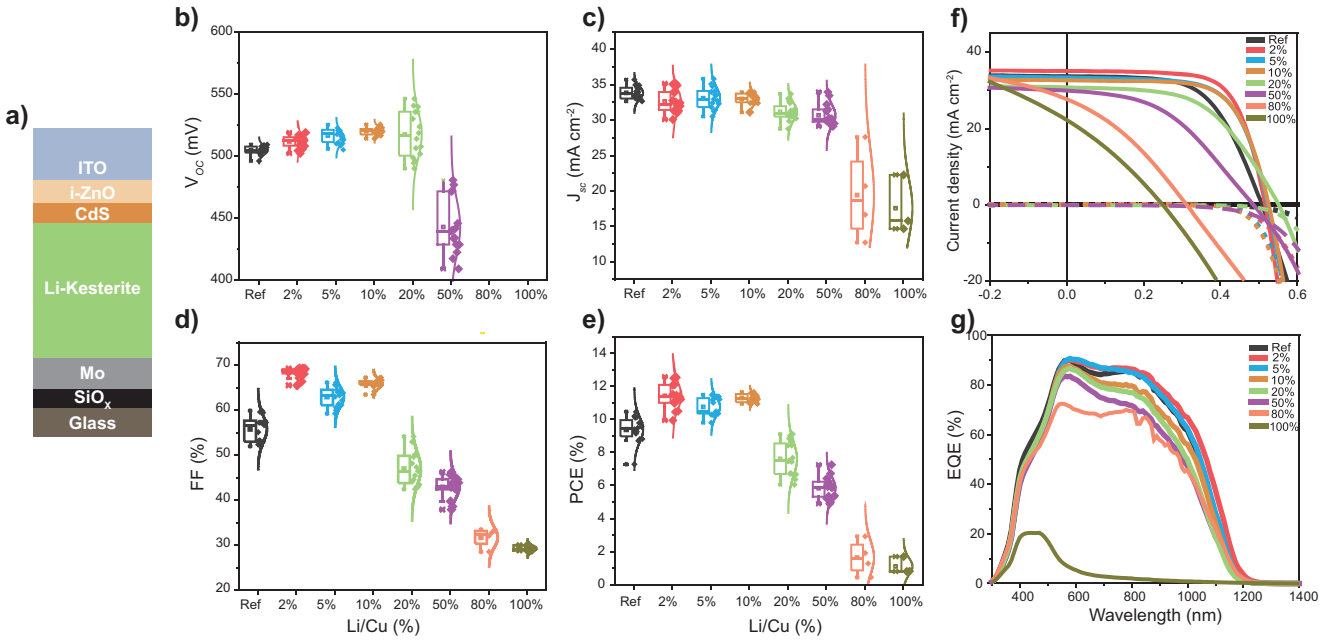

Figure 1. a) Schematic structure of the kesterite device based on a soda lime glass substrate with a SiO_x Na barrier layer. b–e) Statistical distribution of the photovoltaic parameters for devices with varying Li content. f) Representative illuminated and dark *J–V* curves of the devices for varying Li content. g) EQE spectra of the device for varying Li content.

with a Li concentration higher than 20% show a steep decrease in all the optoelectronic parameters.

The diode parameters were obtained by fitting the dark and illuminated current–voltage (*J–V*) curves from the second batch of devices in Figure S1 and Table S1 (Supporting Information) using the single diode method.[32] The results are summarized in **Table 1**. The most relevant change induced by $LiClO_4$ introduction is the significant increase in the shunt resistance (R_{sh}) and reduction in recombination current (J_0) and series resistance (R_s). These changes correlate with the enhancement in fill factor (FF) and open-circuit voltage (V_{OC}) of the devices. The reduction in the R_s value of the 2% Li device probably results from increased absorber conductivity. A reduced transport barrier for the carriers consequence of modified band alignment could also reduce the R_s. These changes could stem from the increased hole concentration by Li incorporation, as shown throughout the paper. For devices with high Li content (>2%), the observed increase in R_s can be attributed to the presence of secondary phases resulting from excessive Li incorporation. The small changes in the ideality factor suggest that the dominant recombination mechanism and the region in the device, the SCR are unchanged by the Li incorporation, suggesting that Li has little influence on the recombination rates.

Table 1. Summary of the single diode parameters extracted from illuminated and dark *I–V* curves, along with the carrier density and space charge region (SCR) width extracted from capacitance-voltage analysis for the devices with the optimal range of Li content.

	0Li	2Li	5Li	10Li
R_s-light (Ohm cm^2)	0.86	0.57	1.21	0.92
R_s-dark (Ohm cm^2)	0.85	0.65	1.34	1.07
R_{sh}-dark (Ohm cm^2)	3345	56642	29837	13463
N	1.5	1.6	1.5	1.5
J0 (A cm^{-2})	6.3E-08	1.8E-08	1.0E-08	1.1E-08
N_{CV} (cm^{-3})	3.4E15	1.2E16	1.0E16	1.2E16
SCR Width (nm)	210	178	191	186

The changes in the current collection are characterized by the external quantum efficiency (EQE) and are presented in Figure 1g, showing an improvement of the transport properties for the samples with Li/(Cu+Ag) from 2% to 5% and a slight decrease for 10% content and thereof, consistently with the *J–V* data. The band-gap energy (E_g) can be extracted from the EQE data and the corresponding Tauc plots are presented in Figure S2 (Supporting Information). With increasing Li content (2% to 20%), E_g gradually rises until reaching 50%, suggesting the formation of Li alloyed $(Li,Ag,Cu)_2ZnSn(S,Se)_4$, causing the observed slight increase in E_g.[33] In this work, the slight change in E_g implies that Li is not extensively incorporated into the kesterite lattice. However, it is evident that the minor change in E_g is not the direct cause of the observed current drop in the *J–V* curve. This will be further discussed throughout the manuscript. Also, it has been previously shown that the implementation of isovalent alloying elements leads to a reduction of the Urbach energy (E_U) and is usually related to improvements in the device performance due to reduced recombination losses.[7,34,35] In this case, the E_U is unchanged suggesting that the grain quality is similar for all the samples, regardless of the Li content, which indicates that the effects induced by Ag on the Cu—Zn disorder dominates over the effects of Li. Therefore, it seems that Li doping is not significantly impacting the grain quality and consequently the changes

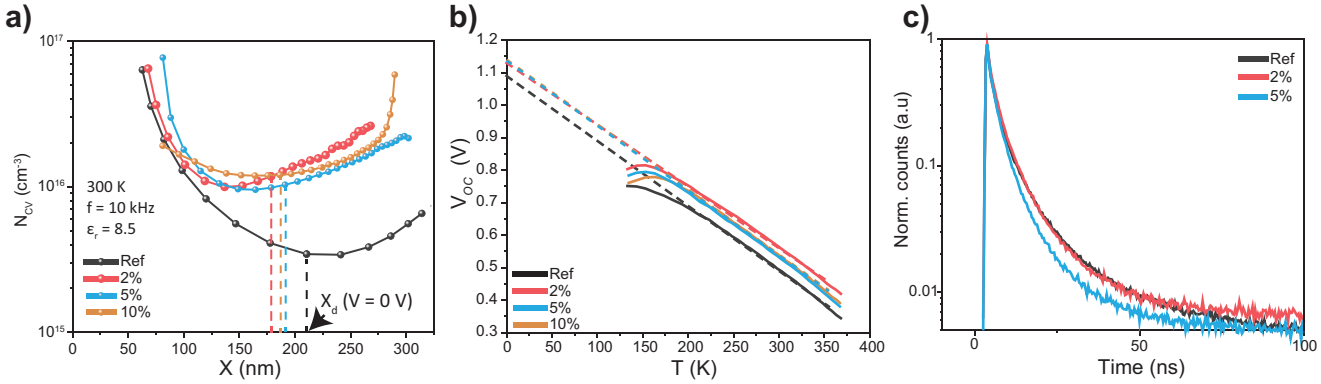

Figure 2. a) Carrier density profiles extracted by C-V analysis. b) Plots of V_{OC} versus temperature (V_{OC}–T) and linear fits of the recombination E_a of the devices. c) TRPL decay for the Ref and low Li content devices.

in the device performance are related to changes in other optoelectronic properties.

The capacitance-voltage profiling analysis shown in **Figure 2a** reveals a clear increase in the apparent carrier concentration (N_{CV}), leading to one order of magnitude increase from 10^{15} to 10^{16} cm^{-3} for the devices with Li content from 2% to 10%, as can be seen in Table 1. The small difference in the *C–V* profiling values close to the junction suggests that the main effect induced by Li incorporation is a bulk-related effect while the interface quality is similar.

To further confirm that, the activation energy (extracted from the extrapolation of the V_{OC} vs T data) as shown in Figure 2b, is practically unchanged with values very close to the E_g showing that, if any, the changes at the interface induced by the Li doping do not have a remarkable impact in the device performance. Nevertheless, the increase in the bulk density of the majority carrier can explain the improvements in the device performance, since, for sufficiently high lifetimes, the measured increase in carrier concentration can lead to a remarkable performance improvement, as demonstrated in the literature.[15,36] Moreover, the impact of alkaline treatments on the intra-grain lifetime and grain boundary recombination rates could be masked by a low carrier concentration.[37] Therefore, the implementation of a Li precursor salt in the solution precursor, leading to ACZTSSe with carrier concentrations near 10^{16} cm^{-3}, is critical to significantly improve the device performance. On the other hand, other bulk properties might be affected by the increase in hole density therefore the impact of Li doping on the minority carrier lifetime should be assessed. Besides the enhanced radiative recombination rates due to an increased hole density, an interplay between lifetime and hole density due to the proliferation of intrinsic donor recombination centres (Sn_{Zn}) if the material is formed under p-type condition has been previously identified.[38–40] Figure 2c shows the TRPL decay of samples with 0, 2, and 5% Li content and a slight decrease of lifetime for the concentration of 5% can be observed. Hence, our investigation reveals that the threshold of Li content required to influence minority carrier lifetime is higher compared to the threshold affecting hole density. Interestingly, the interplay between hole density and lifetime has not been observed for several post-deposition heat treatment (PDT) strategies, which have demonstrated modifications of the hole concentration without detrimental effects on the lifetime and V_{OC}[41,42] In light of these findings, it becomes apparent that the incorporation kinetics of Li in the solution-processed kesterite material is dependent on the Li content. Consequently, further insight into the incorporation mechanism is essential for a comprehensive understanding.

Currently, there is no absolute consensus on the mechanism by which the hole density increases nor is there a universal correlation between carrier density and lifetime due to the complex behavior of kesterite solar cells. However, different mechanisms have been proposed to explain the increase in hole density with alkali doping in Cu-based chalcogenides: i) an increase in the Cu vacancies due to a decreasing Li solubility and the segregation to the grain boundaries during the cooldown or ii) the formation of easily ionized acceptor Li_{Zn} antisites.[19,23,40] In this work, we note that these mechanisms might be valid depending on the initial conditions of the kesterite material and that, furthermore, the effect on the lifetime should be different for both cases. In case (i) it is assumed that the defects are defined during the absorber formation from a chemical reaction at high temperatures. Interestingly, case (i) would affect the lifetime of kesterite since the Li atoms are incorporated in the chalcogenide phase prior to the formation of the material. In case (ii) the kesterite phase is already formed and well-crystalized. Then, only the Cu and Zn defects with much higher mobility can be affected by Li incorporation and change concentrations, leading to a practically unchanged lifetime dominated by the Sn-related defects. This differentiation stems from the substantial disparity in activation energies required for Sn diffusion in the kesterite material as compared to that of Cu and Zn. The different transition temperatures for the Cu—Zn disordered kesterite phase (at 200–250 °C) and the Cu–Zn–Sn disordered cubic phase (1000 °C) provide clear evidence of this characteristic.[43] Therefore, we refer to the terms formation-like for case (i) and PDT-like for case (ii). In this work, the lifetimes of the samples with 2% Li remained unchanged compared to the reference samples, however, the hole density of the 2% and 5% samples are similar, suggesting that the recombination centre density of the 2% Li sample is similar to the reference case while the shallow acceptor defect density is increased. This hints at a PDT-like Li effect for low Li/(Cu+Ag) ratios which becomes increasingly more formation-like with increasing Li content, which clearly implies that the kinetics of Li incorporation is affected by the Li concentration. To understand the underlying mechanism

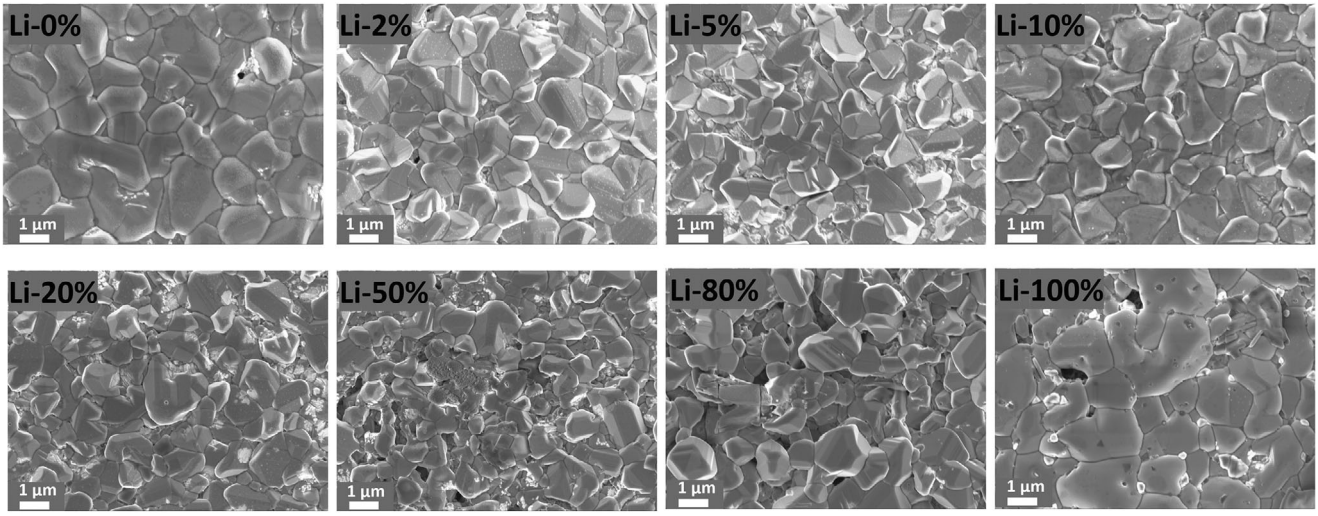

Figure 3. Top-view scanning electron microscopy images of the absorbers with varying amounts of added $LiClO_4$ in the precursor solution.

driving the N_{CV} increase with different effects in the minority carrier lifetime further characterization is necessary to shed light on the role of Li during the high-temperature step.

It has been previously reported that the addition of alkali in the kesterite system leads to a performance improvement correlated to morphology improvements for formation-like alkali incorporation.[27,36] However, a decoupling of the efficiency enhancements due to changes in optoelectronic properties and the morphology effect with evaporated NaF doping, revealing that the former had a more significant contribution via an increase in the hole density from 10^{15} to 10^{16} cm^{-3}.[44] It is thus also necessary here to assess the influence of morphology first to properly understand the observed PCE improvements. It has been previously demonstrated that the introduction of Ag has a significant impact on grain size and morphology.[7,45] The effects of Li incorporation on the absorber morphology for different concentrations are shown in **Figure 3**, with almost no impact observed for concentrations below 20% indicating that, if present during the grain crystallization, the Li-(S,Se) phases do not have a direct impact on the grain growth mechanism, confirming that the dominant grain growth mechanism is not affected by the presence of chalcogen-rich and low melting point phases or the incorporation of Li in the lattice. This hints at a PDT-like behavior, where the Li content only affects the shallow defect structure of the material. In contrast, the samples with Li/(Cu+Ag) above 50%, show bigger grains as well as a morphology degradation. These results are typically observed with the introduction of high concentrations of alkali chalcogenide species.[21] It has been previously shown that the formation of the top grains occurs during the first stages of the high temperature step.[6]

Therefore, as shown in Figure 3 and Figure S3 (Supporting Information), the unchanged morphology of low Li content samples suggests that the formation of Li–Se phases is posterior to the top grain growth. When the Li content is sufficient, the formation of Li–Se phases seems to be accelerated, being able to impact the morphology of the absorber film. It has been reported that high concentrations of Li introduction can lead to the formation of Li-alloyed kesterite by substituting the Cu position.[33] In this investigation, introducing Li without reducing the concentrations of Cu and Ag may lead to an overabundance of [I] elements in the film. This elucidates why the 100% Li films display a large and compact grain morphology, as depicted in Figure 3, yet exhibit a lack of PV performance in the device.

The Li loss during the different stages of the processing of kesterite materials has been reported previously.[21] It is well-known that due to the inability of Li to complex with thiourea major loss of Li is observed during the spin-coating of the precursor film due to the volatilization of uncoordinated metal-chloride compounds. Also, Li re-dissolution during the deposition of the following layers has been observed.[21] In this work, we characterize the different Li content by ICP-MS for the different Li composition targets, the results of which are presented in Table S2 (Supporting Information). Aside from the outlier behavior observed in samples with lower Li content, the use of $LiClO_4$ as the Li precursor, instead of LiCl, led to approximately an order of magnitude higher Li detection in the absorber at similar molecular inks concentrations (e.g., 20%), compared to the literature.[21] This phenomenon can be attributed to the very low hygroscopicity of $LiClO_4$, preventing substantial loss of Li during re-spin coating. In previous studies, LiCl doping solutions were spin-coated in ambient air. We speculate that the loss of Li is facilitated by LiCl's ability to readily absorb moisture from the air, forming LiCl-H_2O microdroplets that easily mix with DMSO, leading to significant Li loss during the re-spin-coating process. Also, the Li present in the precursor film is expected to be in the $LiClO_4$ phase which has high thermal stability, with thermal decomposition starting at temperature of 420°C and peaking at 500°C, well beyond those used during spin-coating and similar to the selenization highest setpoint.[46] Finally, a minor Li loss during the CdS deposition has been reported and is also observed in this work, as shown in Table S3 (Supporting Information), showing that excess Li can be dissolved during the CBD, suggesting that excess Li is removed during this process. To assess the distribution of Li during the grain growth stage the Li content of the absorber films prior to the CdS deposition and after the CdS+JHT has been characterized by ToF-SIMS and presented in Figure S4a (Supporting

Information), the distribution of Li over any of the other metals (Cu, Ag, Zn, and Sn) changes with Li concentration. The Li content of the samples is homogeneously distributed across the absorber. In the case of the 2% samples, the distribution remains unchanged after the CdS+JHT, indicating that the Li is effectively incorporated in the kesterite lattice. When the Li content is increased to 5%, the ToF-SIMS shows a reduction in signal after the CdS+JHT, suggesting that excess Li segregates in the film as a secondary phase, which is (at least partially) dissolved during the CBD. The high thermal stability of $LiClO_4$ can prevent its decomposition during the first stages of the thermal process, which are also more chalcogen-poor (and therefore the formation of Li–Se phases is not displaced toward the product).[46] Also, it has been previously shown that the formation of ACZTSSe topmost layer occurs within the first minutes of the high-temperature step.[6] The observed Li loss from the CBD process but the unchanged ToF-SIMS profile for the 2% Li content suggests that (naturally) Li–Se phases are formed at the surface and incorporate to ACZTSSe diffusing from the top, consistently with the unidentified phase observed in the SEM top-view of Figure 3. Also, the reduced J_{sc} with increasing Li content could be explained by the parasitic absorption of secondary phases. Therefore, the Li incorporation, typically expected from Li–Se liquid phases, seems to be posterior to the top grain growth and kinetically limited by the down-diffusion and reaction of Li–Se phases with the kesterite absorber at the surface and grain boundaries, leading to remaining unreacted Li–Se phases within the absorber film. The PL emission peaks measured in the ACZTSSe-Li/CdS (w/JHT) configuration are shown in Figure S4b (Supporting Information) and show a slight blueshift at 5% content, which is related to an increase in the E_g due to Li incorporation.

Besides the determination of how much Li is incorporated in the absorber material, it is also important to understand the lattice position occupation of the Li atoms and its effects on the distribution of other cations such as Ag, Cu, and Zn. Even though Li has the highest solubility in CZTSSe among all the alkali it is still relatively low. Then, excess Li can form Li–Se phases and partially displace Cu or Zn to other kesterite lattice positions. Completely understanding these effects is complex since we explore for the first time the effects of triple cation competition in kesterite materials by changing the Li/(Li+Cu+Ag) ratio from Li-poor (0.017) to Li-rich (0.43). The competition of the Cu, Zn, Ag, and Li atoms for the occupation of Cu and Zn positions will result in a complex interplay with the increasing Li content. In this sense, due to the large Ag atomic size, the formation energy of Ag_{Zn} is much higher compared to the formation of Cu_{Zn} and Li_{Zn} antisites. Therefore it can be assumed that only Ag_{Cu} defects are formed and that their concentration is not affected by the Li content.[18,23] Li will naturally tend to occupy Cu positions by forming Li_{Cu} neutral defects, which have been found to show negative formation energy in ab initio studies, indicating the spontaneous formation of this defect for the dilute limit.[23] The charge neutrality of the Li_{Cu} defect implies a formation energy independent from the Fermi energy and therefore only the composition will determine the concentration of this defect. The effects of the chemical potential of Cu on the alkali incorporation have been studied by Haass et al,[27] showing that a Li-induced increase in E_g could only be achieved in Cu-poor compositions. Also, the presence of Li_{Zn} defects is expected in our samples, consistently with its low formation energy, which is further reduced in intrinsic low p-type growth conditions. Besides, the different antisites that can be formed in the kesterite lattice may have a completely different impact on the optoelectronic parameters of the material as well as a different response in the Raman spectra. The Raman spectra obtained for all the devices are shown in Figure S5a (Supporting Information). First, in **Figure 4a** we show the position of the main peak of (A)CZT(S)Se with the different

Li/(Cu+Ag) ratios. The peak typically centered ≈196 cm^{-1} corresponds to Se–Se vibrations and similar peaks can be detected for many Se-based compounds. The incorporation of Li tends to shift the peaks toward higher wavenumbers, indicating the incorporation of a lighter element in the lattice. Surprisingly, for concentrations above 50%, the position of the peak starts to shift toward lower wavenumbers indicating the segregation of two phases. The area of the 176 cm^{-1} peak shown in Figure 4b presents a similar behavior and is correlated to a decreasing density of the $[V_{Cu}+Zn_{Cu}]$ defect cluster.[47] It can be easily observed that the density of this cluster increases up to 50%, then drastically decreasing up to 100% Li content. Therefore, a decreased density of $[V_{Cu}+Zn_{Cu}]$ in the system induced by the Li incorporation can be concluded. The formation of Li_{Cu} by a reduction of the concentration of V_{Cu} is consistent with the slight increase in E_g and is therefore likely confirmed by this analysis. However, an increased density of the Zn_{Cu} defects due to the Li_{Zn} formation and displacement of Zn and/or Cu from Zn positions could also be influencing the area of the 176 cm^{-1} peak. To verify this, the area of the 250 cm^{-1} peak is analyzed and correlated to an increasing density of the $[Zn_{Sn}+2Zn_{Cu}]$ (ZnSe-like) defect cluster higher Li content as shown in Figure 4c.[47] The area of this peak directly increases up to 80% Li content and then drops to very low values at 100% Li content. The latter indicates an increased content of Zn out of its lattice position, suggesting the increased presence of Li in Zn positions. Therefore, a reduced density of V_{Cu} and an increased density of Zn_{Cu} defects can be extracted from the Raman peak area analysis. It has been previously shown that an increase in the concentration of acceptor Li_{Zn} defects can have first order impact in the hole density due to very low formation and ionization energies. Furthermore, the formation of Li_{Zn} could also reduce the density of less ionizable Cu_{Zn} defects since the measured reduction of the V_{Cu} could be related to the formation of both Li_{Cu} and Cu_{Cu}. The stabilization of Zn_{Cu} with increasing Li content is expected due to free charge self-compensation effects, which would justify the saturation of hole concentration for higher Li contents. Therefore, according to the Raman analysis, the shallow defect driving the increase of hole density in Li-doped ACZTSSe are not V_{Cu} which seems to be reduced in density and neither Zn_{Cu} which is increasing in concentration. Therefore, the most likely option is an increase in the Li_{Zn} defect density. Cu_{Zn} defects could be also present in higher concentrations, however, considering their high ionization energy and the tendency to form $[Cu_{Zn}+Zn_{Cu}]$ clusters it is becomes a less plausible option. Certainly, the formation of Li_{Zn} is likely the main reason for the increase in carrier concentration observed in the CV profile. Li_{Zn} also has the potential to mitigate the Fermi level pinning issues at the Kesterite/CdS interface, but further investigations are needed. These results indicate that the incorporation mechanism of Li introduces an additional shallow

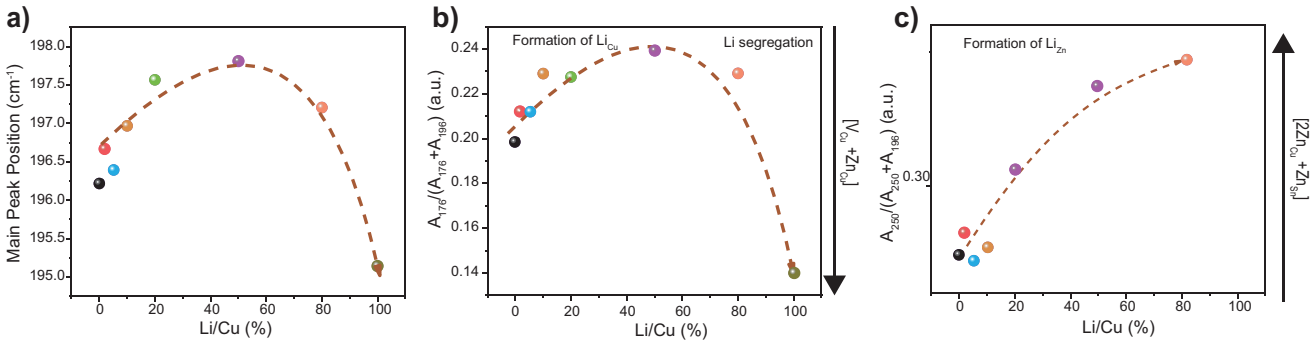

Figure 4. a) Plot of the ACZTSSe main peak position in Raman spectra as a function of Li content. b) Plot of the area ratio of the 176 cm^{-1} peak to the main peak. c) Plot of the area ratio of the 250 cm^{-1} peak to the main peak.

defect state without impacting the morphology, that is, PDT-like mechanism, consistently with all the previous results.

Hence, the incorporation of Li in Cu and Zn positions seems evident, however, an outlier behavior for the Li5% and Li10% samples is observed and could be explained by a weak contribution to the A_{196} from the overlapping of a Sn–Se phase-related peak, which also correlates to the emergence of two peaks centered at ≈95 and 125 cm^{-1} for Li concentrations of 10% and above. Furthermore, the intensity of the peak at 95 cm^{-1} shown in Figure S5b (Supporting Information) increases proportionally with the Li content, hence, an expected presence of a Sn-related secondary phase is expected. The only reasonable explanation for this behavior is an enhanced decomposition of the absorber induced by excess Li, as indicated by an enhanced Sn-loss detected by ICP-MS shown in Table S2 (Supporting Information), which is known to be related to the formation volatile of Sn–Se species, consistently with the observed morphological changes. The formation of $SnSe_2$ species for high alkali contents has been previously reported in the kesterite system.[22]

Therefore, with the presented characterization and the effects observed in previous studies, understanding the Li dynamics from the solution to the final device is possible. In the solution, Li cannot form complexes with thiourea, so Li is present as solvated $LiClO_4$ in the precursor solution. Due to the high decomposition temperature (420 °C) of $LiClO_4$, the incorporated Li is primarily present as $LiClO_4$ in the precursor film.[46] As described in step 1 of **Figure 5**, the $LiClO_4$ present in the precursor film decomposes and reacts with Se during the thermal treatment ramp starting above 420°C, following the reactions outlined below:

$$LiClO_{4(s)} \rightarrow LiCl_{(s)} + 2O_{2(g)} \quad (1)$$

$$2LiCl_{(s)} + Se_{(g)} \rightarrow Li_2Se_{(s)} + Cl_{2(g)} \quad (2)$$

According to the Li–Se phase diagram, the Li_2Se phase can form a liquid phase at the used annealing temperatures for Se-rich conditions. The high thermal stability of $LiClO_4$ and the Se poor conditions during the ramp lead to the formation of liquid Li–Se phases during the first stages of the high-temperature step, which could be consumed by already crystallized ACZTSSe following Equations (3) and (4), as shown in step 2 of Figure 5. The formation of liquid Li–Se phases and the subsequent reaction with the kesterite material at high temperatures explains the delayed incorporation of significant quantities of Li in the kesterite phase after the crystallization is completed, as denoted in step 3 of Figure 5, consistently with the increased hole density without impacting the lifetime and the unchanged morphology, explaining the PDT-like behavior of the system for low Li contents. Also, it seems that with increasing Li content the incorporation of Li is accelerated, hinting that low Li concentration is necessary to control the kinetics of Li incorporation prior to the grain formation. Naturally, during the cool-down stage, the Li solubility is decreased by temperature and the excess Li will be segregated to the grain boundaries and surface, however, this effect does not seem to dominate the hole concentration in this system.

$$Li_2Se_{(s)} + Se_{x(g)} \rightarrow Li_xSe_{(l)} \quad (3)$$

$$2Li_xSe_{(l)} + (Ag, Cu)_2ZnSn(S, Se)_{4(s)} \rightarrow (Li_x, Ag, Cu)_2ZnSn(S, Se)_{4(s)} + 2Se_{(g)} \quad (4)$$

Hence, according to the proposed model, based on the experimental observations, the Ag-alloying determines the recrystallization mechanism, crystalline quality, and disorder level of the kesterite material, while Li doping does only contribute to an increase in the hole density. It has been previously demonstrated that Ag alloying contributes to a reduction of Cu_{Zn} defects while the density of V_{Cu} and Zn_{Cu} defects remains constant.[46] Besides the well-known formation of Li_{Cu} defects, the Ag-induced reduction of Cu_{Zn} defects enables the efficient incorporation of Li in unoccupied Zn positions, increasing the hole density. Hence, the synergistic interaction between Li and Ag enhances the formation of beneficial Li_{Zn} shallow acceptor defects, enabling optimal hole densities for solar cell performance.

For the Li-rich conditions (above 20%), the presence of Li_2Se phase is also expected as an intermediate. The small density of the Li_2Se phase (1.66 g cm^{-3}), compared to $LiClO_4$ and LiCl (2.42 and 2.07 g cm^{-3}, respectively), combined with the much higher content of $LiClO_4$ in the precursor film, can result in the formation of micro- or nano-sized Li_2Se grains. These grains may react with the chalcogen gas and the kesterite material before ACZTS recrystallization, capturing Sn and forming Li-intercalated Sn(S,Se) species. These species are susceptible to volatilization, explaining the enhanced Sn and Li loss, as well as

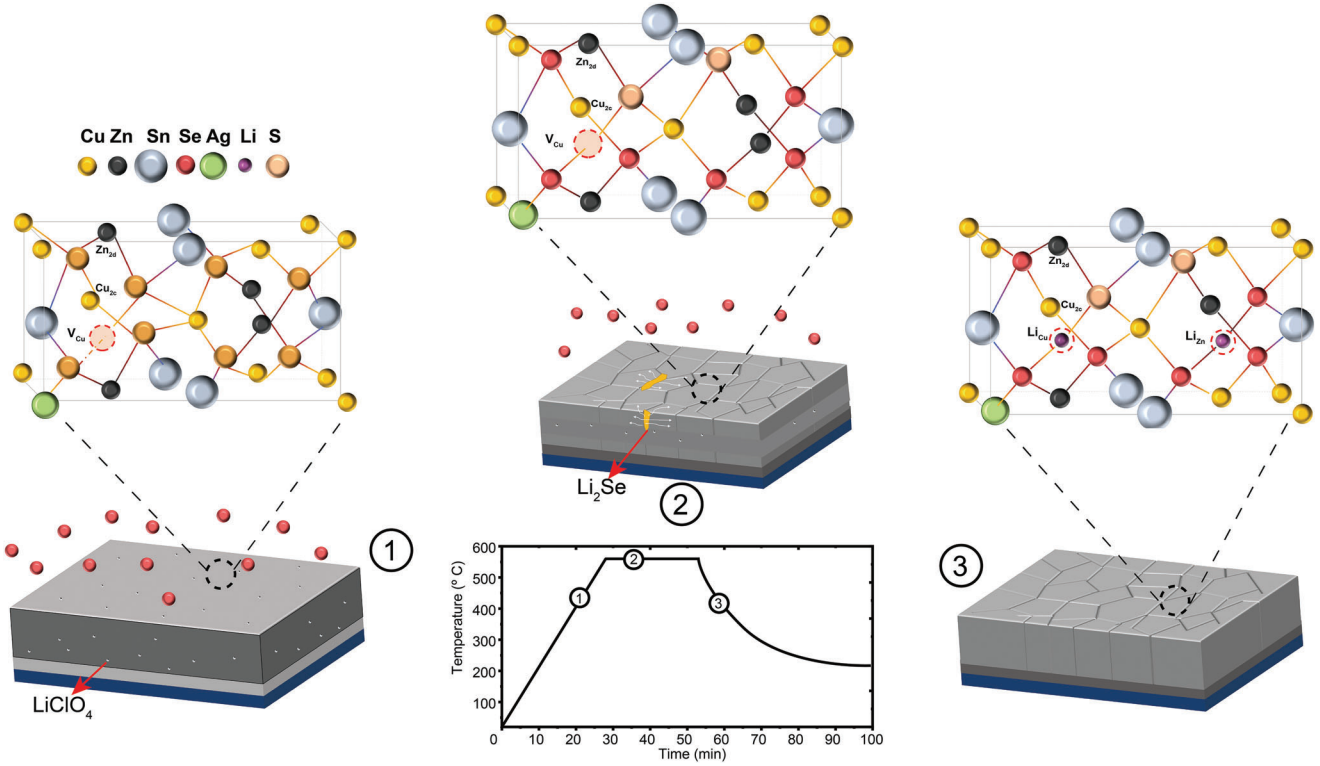

Figure 5. Schematic of the Li incorporation dynamics during the selenization step in a atomic scale (top) and macroscopic scale (bottom). In (1), the conditions during the heating ramp are schematized, the Se is evaporated forming a saturated Se atmosphere and the amorphous ACZTS layer and the $LiClO_4$ inclusions remain unreacted. In (2), during the first minutes of the dwelling step, the re-crystallization of the top and bottom layers is started. Simultaneously, the $LiClO_4$ in the film decomposes and reacts with Se forming Li–Se phases. The Li–Se phases are consumed during the posterior stages of the dwelling, where Li incorporates in the kesterite lattice forming Li_{Cu} and Li_{Zn} defects of (3).

the presence of voids and pinholes and the larger, less faceted grains.

After the detailed study of the influence of $LiClO_4$ as Li precursor salt in high-efficiency ACZTSSe in DMSO, the method has been transferred to similar solvents such as 2-methoxyethanol (MOE) and N,N-dimethylformamide (DMF), which are known to result in practically identical amorphous precursor film.[5,6,48] The utilization of DMF and MOE solvents facilitates the spin-coating process in an ambient atmosphere. It is noteworthy that all characterizations conducted in this study were performed on samples prepared using DMSO as a solvent. When combined with optimized window layer deposition, this approach results in a maximum device performance of 14.1% with MOE as the solvent. The *J*—*V*, EQE, and CV data of the device is shown in **Figure 6**. The reproducibility of the process and its statistical significance have been assessed by repeating the same process several times and monitoring the optoelectronic parameters of every batch. The improvement in all the optoelectronic parameters upon the implementation of Li doping can be observed in **Figure 7**. The small dispersion in the measured optoelectronic

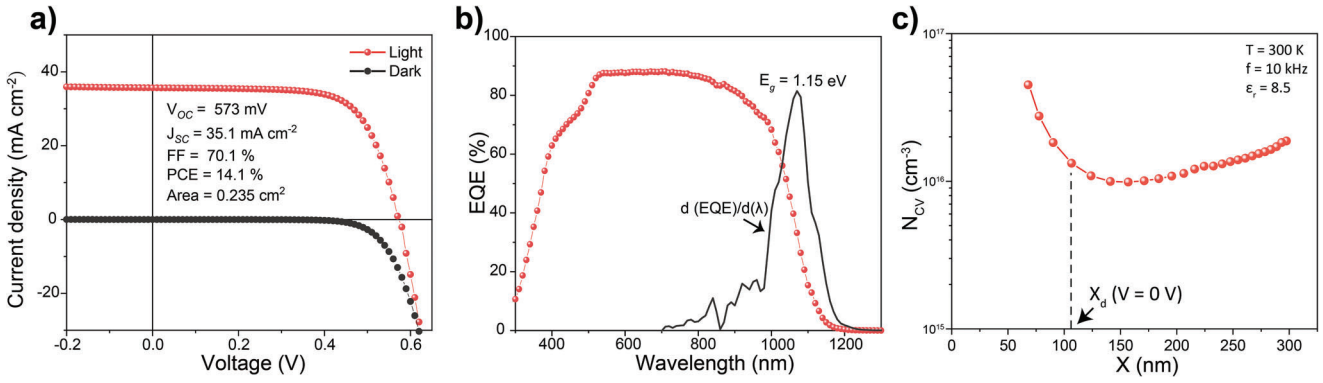

Figure 6. a) Light and dark *J*–*V* curves, b) EQE and c) C-V profile of the champion ACZTSSe-Li device.

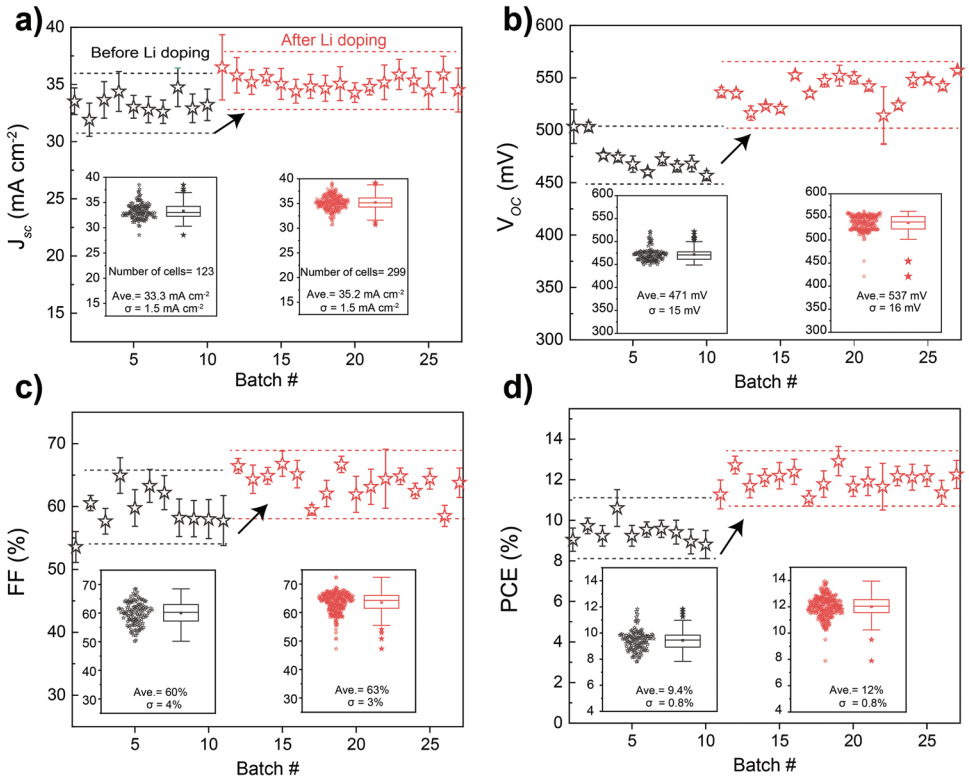

Figure 7. PV parameters of different batches of device before and after the implementation of optimal Li doping conditions: a) J_{SC}, b) V_{OC}, c) FF, and d) PCE. Dashed lines are included as visual aid.

parameters reveals the resilience of the method to batch-to-batch variations. The implementation of Li-doping leads to a remarkable average efficiency of 12% for almost 300 cells.

In recent years, as shown in **Figure** 8a, the implementation of Ag alloying together with other extrinsic doping and alloying agents has been key to achieve high-efficiency kesterite solar cells. In this work, we demonstrate that the introduction of Li as a co-dopant leads to record efficiencies with the highest V_{OC} for Se-rich kesterite materials (573 mV). The voltage deficit ($V_{OC}^{def} = V_{OC}^{SQ} - V_{OC}^{Measured}$, where $V_{OC}^{SQ} = 0.932 \cdot E_g/q - 0.1667$ V) of the champion device of this work is one of the lowest among the literature, and the lowest for its bandgap ($E_g = 1.15$ eV) as shown in Figure 8b, indicating the high quality of the material and the optimized device performance. Further improvement could be achieved by the implementation of anti-reflective coating (ARC) increasing the J_{SC} by at least 1 mA cm^{-2}, leading to a projected efficiency of 14.5%.

3. Conclusion

In conclusion, this work demonstrates that the incorporation of high solubility group I element Li via easily dissolved and

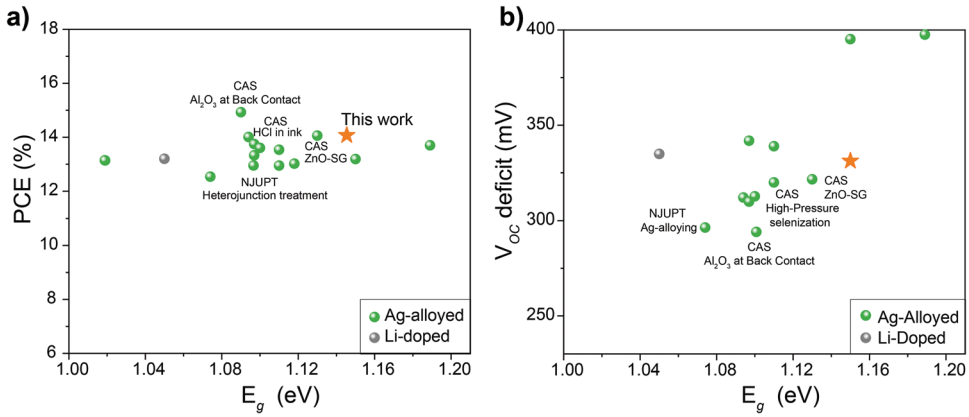

Figure 8. a) Record efficiencies of kesterite solar cells as a function of E_g. b) V_{OC} deficit of the corresponding devices as a function of E_g.

thermally stable $LiClO_4$ can be adopted to enhance the hole density of Ag-alloyed kesterite material without severely impacting the lifetime. Consequently, this brings large performance improvements and raises the efficiency limit for strategies aiming to increase the effective minority carrier lifetime. The performed characterization reveals that the beneficial changes in crystal quality, morphology, and cation disorder induced by Ag-alloying remain unchanged with the Li incorporation. The interplay between Ag-alloying, reducing the density of Cu_{Zn} defects, and Li-doping, seemingly promoting the formation of beneficial Li_{Zn} defects, enables devices with PCEs above 14%. These findings demonstrate that both multinary and isovalent doping and alloying are critical to tune and improve the properties of kesterite absorbers for photovoltaic applications.

Supporting Information

Supporting Information is available from the Wiley Online Library or from the author.

Acknowledgements

This project received funding from the European Union's H2020 research and innovation programme under grant agreement number 952982 (CUSTOM-ART) and 866018 (SENSATE), and by the Science Ministry of Spain projects number PID2020-116719RB-C41 (MATER-ONE) and TED2021-130265B-C21 (MIRACLE). The authors from UPC and IREC belong to the Micro and Nanotechnologies for Solar Energy Group (MNT-Solar) Consolidated Research Group of the "Generalitat de Catalunya" (2021 SGR 01286). A.J.A. thanks the European Social Fund+ for the FI fellowship. S.G. thanks the Juan de la Cierva grant IJC2020-044716-I funded by MCIN/AEI/10.13039/501100011033 and by the European Union NextGenerationEU/PRTR. E.S. is grateful to ICREA Academia program. R.S. thanks FWO for the funding through the Fundamental Research PhD Fellowship (1178024N) and Travel Grant for a long stay abroad (V462623N). A.B. thanks the grant SIR/2022/001011 by SERB India. H.X. thanks the support from National Key Research and Development Program of China (2019YFE0118100).

Conflict of Interest

The authors declare no conflict of interest.

Author Contributions

Y.G. and A.J.A contributed equally to this work. Y.G. performed conceptualization, methodology, formal analysis, investigation, data curation, visualization, and writing original draft; A. A. performed conceptualization, formal analysis, investigation, data curation, visualization, and writing original draft; A.G.M. performed formal analysis and data curation; S.M. performed methodology and data curation; A.B. performed methodology, and data curation; R.S. performed methodology and investigation of data curation; R.C. supervision; D. Flandre: supervision; B.V. carried out supervision; S.G. performed Investigation; H.X. performed Supervision, writing–review, and editing; A.P.R. performed supervision, funding acquisition E.S. performed supervision, conceptualization, writing–review, and editing, funding acquisition.

Data Availability Statement

The data that support the findings of this study are available from the corresponding author upon reasonable request.

Keywords

Cu2ZnSn(S,Se)4, CZTSSe, kesterite solar cells, molecular inks route, thin film chalcogenides

Received: March 18, 2024
Revised: April 24, 2024
Published online: June 7, 2024

[1] S. Giraldo, Z. Jehl, M. Placidi, V. Izquierdo-Roca, A. Pérez-Rodríguez, E. Saucedo, *Adv. Mater.* **2019**, *31*, 1806692.
[2] A. Zakutayev, J. D. Major, X. Hao, A. Walsh, J. Tang, T. K. Todorov, L. H. Wong, E. Saucedo, *J. Phys. Energy* **2021**, *3*, 032003.
[3] W. Wang, M. T. Winkler, O. Gunawan, T. Gokmen, T. K. Todorov, Y. Zhu, D. B. Mitzi, *Adv. Energy Mater.* **2014**, *4*, 1301465.
[4] Y. Gong, Q. Zhu, B. Li, S. Wang, B. Duan, L. Lou, C. Xiang, E. Jedlicka, R. Giridharagopal, Y. Zhou, Q. Dai, W. Yan, S. Chen, Q. Meng, H. Xin, *Nat. Energy* **2022**, *7*, 966.
[5] Y. Gong, Y. Zhang, E. Jedlicka, R. Giridharagopal, J. A. Clark, W. Yan, C. Niu, R. Qiu, J. Jiang, S. Yu, S. Wu, H. W. Hillhouse, D. S. Ginger, W. Huang, H. Xin, *Sci. China Mater.* **2021**, *64*, 52.
[6] Y. Gong, Y. Zhang, Q. Zhu, Y. Zhou, R. Qiu, C. Niu, W. Yan, W. Huang, H. Xin, *Energy Environ. Sci.* **2021**, *14*, 2369.
[7] Y. Gong, R. Qiu, C. Niu, J. Fu, E. Jedlicka, R. Giridharagopal, Q. Zhu, Y. Zhou, W. Yan, S. Yu, J. Jiang, S. Wu, D. S. Ginger, W. Huang, H. Xin, *Adv. Funct. Mater.* **2021**, *31*, 2101927.
[8] J. Zhou, X. Xu, H. Wu, J. Wang, L. Lou, K. Yin, Y. Gong, J. Shi, Y. Luo, D. Li, H. Xin, Q. Meng, *Nat. Energy* **2023**, *8*, 526.
[9] X. Xu, J. Zhou, K. Yin, J. Wang, L. Lou, M. Jiao, B. Zhang, D. Li, J. Shi, H. Wu, Y. Luo, Q. Meng, *Nat. Commun.* **2023**, *14*, 6650.
[10] Z. Yu, C. Li, S. Chen, Z. Zheng, P. Fan, Y. Li, M. Tan, C. Yan, X. Zhang, Z. Su, G. Liang, *Adv. Energy Mater.* **2023**, *13*, 2300521.
[11] R. Scaffidi, G. Birant, G. Brammertz, J. de Wild, D. Flandre, B. Vermang, *J. Mater. Chem. A* **2023**, *11*, 13174.
[12] M. Neuschitzer, M. E. Rodriguez, M. Guc, J. A. Marquez, S. Giraldo, I. Forbes, A. Perez-Rodriguez, E. Saucedo, *J. Mater. Chem. A* **2018**, *6*, 11759.
[13] X. Pan, X. Li, Y. Yang, C. Xiang, A. Xu, H. Liu, W. Yan, W. Huang, H. Xin, *Adv. Energy Mater.* **2023**, *13*, 2301780.
[14] X. Zhao, Y. Pan, W. Chen, W. Yang, Q. Zeng, L. Li, X. Liao, Z. Zhang, S. Liu, Y. Lai, F. Liu, *Adv. Funct. Mater.* **2023**, *33*, 2301377.
[15] J. Li, J. Huang, F. Ma, H. Sun, J. Cong, K. Privat, R. F. Webster, S. Cheong, Y. Yao, R. L. Chin, X. Yuan, M. He, K. Sun, H. Li, Y. Mai, Z. Hameiri, N. J. Ekins-Daukes, R. D. Tilley, T. Unold, M. A. Green, X. Hao, *Nat. Energy* **2022**, *7*, 754.
[16] W. Chen, D. Dahliah, G.-M. Rignanese, G. Hautier, *Energy Environ. Sci.* **2021**, *14*, 3567.
[17] S. Chen, A. Walsh, X.-G. Gong, S.-H. Wei, *Adv. Mater.* **2013**, *25*, 1522.
[18] Z.-K. Yuan, S. Chen, H. Xiang, X.-G. Gong, A. Walsh, J.-S. Park, I. Repins, S.-H. Wei, *Adv. Funct. Mater.* **2015**, *25*, 6733.
[19] Z.-K. Yuan, S. Chen, Y. Xie, J.-S. Park, H. Xiang, X.-G. Gong, S.-H. Wei, *Adv. Energy Mater.* **2016**, *6*, 1601191.
[20] T. Maeda, A. Kawabata, T. Wada, *Phys. Status Solidi C* **2015**, *12*, 631.
[21] A. Cabas-Vidani, S. G. Haass, C. Andres, R. Caballero, R. Figi, C. Schreiner, J. A. Márquez, C. Hages, T. Unold, D. Bleiner, *Adv. Energy Mater.* **2018**, *8*, 1801191.
[22] Y. E. Romanyuk, S. G. Haass, S. Giraldo, M. Placidi, D. Tiwari, D. J. Fermin, X. Hao, H. Xin, T. Schnabel, M. Kauk-Kuusik, P. Pistor, S. Lie, L. H. Wong, *J. Phys Energy* **2019**, *1*, 044004.
[23] M. He, X. Zhang, J. Huang, J. Li, C. Yan, J. Kim, Y.-S. Chen, L. Yang, J. M. Cairney, Y. Zhang, S. Chen, J. Kim, M. A. Green, X. Hao, *Adv. Energy Mater.* **2021**, *11*, 2003783.

[24] Z. Shen, S. Wang, Y. Liu, Y. Sun, J. Wu, H. Guo, K. Zhang, S. Zhang, F. Liu, Y. Zhang, *J. Energy Chem.* **2021**, *62*, 637.
[25] H. Xin, S. M. Vorpahl, A. D. Collord, I. L. Braly, A. R. Uhl, B. W. Krueger, D. S. Ginger, H. W. Hillhouse, *Phys. Chem. Chem. Phys.* **2015**, *17*, 23859.
[26] J. Zhou, X. Xu, B. Duan, H. Wu, J. Shi, Y. Luo, D. Li, Q. Meng, *Nano Energy* **2021**, *89*, 106405.
[27] S. G. Haass, C. Andres, R. Figi, C. Schreiner, M. Bürki, Y. E. Romanyuk, A. N. Tiwari, *Adv. Energy Mater.* **2018**, *8*, 1701760.
[28] Y. Liu, C. Hu, Y. Qi, W. Zhou, D. Kou, Z. Zhou, L. Han, Y. Meng, S. Yuan, S. Wu, *Adv. Mater. Interfaces* **2022**, *9*, 2201677.
[29] J. Tong, S. Wang, G. Wang, Y. Liu, Y. Wang, L. Chen, L. Wang, D. Pan, X. Zhang, Y. Liu, *Sol. Energy* **2021**, *220*, 882.
[30] T. Gershon, Y. S. Lee, P. Antunez, R. Mankad, S. Singh, D. Bishop, O. Gunawan, M. Hopstaken, R. Haight, *Adv. Energy Mater.* **2016**, *6*, 1502468.
[31] Y. Yang, L. Huang, D. Pan, *ACS Appl. Mater. Interfaces* **2017**, *9*, 23878.
[32] S. S. Hegedus, W. N. Shafarman, *Prog Photovolt: Res. Appl* **2004**, *12*, 155.
[33] Y. Yang, X. Kang, L. Huang, D. Pan, *ACS Appl. Mater. Interfaces* **2016**, *8*, 5308.
[34] J. Chantana, Y. Kawano, T. Nishimura, A. Mavlonov, T. Minemoto, *Sol. Energy Mater. Sol. Cells* **2020**, *210*, 110502.
[35] C. Yan, K. Sun, J. Huang, S. Johnston, F. Liu, B. P. Veettil, K. Sun, A. Pu, F. Zhou, J. A. Stride, M. A. Green, X. Hao, *ACS Energy Lett.* **2017**, *2*, 930.
[36] M. F. M. Fathil, M. K. M. Arshad, U. Hashim, A. R. Ruslinda, R. M. Ayub, A. H. Azman, M. Nurfaiz, M. Z. M. Kamarudin, M. Aminuddin, A. R. Munir, 2014 IEEE International Conference on Semiconductor Electronics (ICSE2014), Kuala Lumpur, August, **2014**, pp. 24.
[37] X. Chang, J. Fu, D. Kou, W. Zhou, Z. Zhou, S. Yuan, Y. Qi, Z. Zheng, S. Wu, *J. Mater. Chem. A*, *9*, 413.
[38] S. Kim, J. A. Márquez, T. Unold, A. Walsh, *Energy Environ. Sci.* **2020**, *13*, 1481.
[39] J. Li, Z.-K. Yuan, S. Chen, X.-G. Gong, S.-H. Wei, *Chem. Mater.* **2019**, *31*, 826.
[40] A. Jimenez-Arguijo, A. Navarro Güell, Y. Sanchez, C. Malerba, M. Valentini, P. Becker, L. Choubrac, T. Unold, Z. Jehl Li-Kao, S. Giraldo, E. Saucedo, *Sol. RRL* **2022**, *6*, 2200580.
[41] S. Bourdais, C. Choné, B. Delatouche, A. Jacob, G. Larramona, C. Moisan, A. Lafond, F. Donatini, G. Rey, S. Siebentritt, A. Walsh, G. Dennler, *Adv. Energy Mater.* **2016**, *6*, 1502276.
[42] A. Jimenez-Arguijo, I. Cano, F. Atlan, Y. Gong, K. J. Tiwari, M. Placidi, J. Puigdollers, Z. Jehl Li-Kao, E. Saucedo, S. Giraldo, *Sol. Energy* **2023**, *262*, 111883.
[43] S. P. Ramkumar, A. Miglio, M. J. van Setten, D. Waroquiers, G. Hautier, G.-M. Rignanese, *Phys. Rev. Materials* **2018**, *2*, 085403.
[44] C. Andres, T. Schwarz, S. G. Haass, T. P. Weiss, R. Carron, R. Caballero, R. Figi, C. Schreiner, M. Bürki, A. N. Tiwari, Y. E. Romanyuk, *Sol. Energy* **2018**, *175*, 94.
[45] C. J. Hages, M. J. Koeper, R. Agrawal, *Sol. Energy Mater. Sol. Cells* **2016**, *145*, 342.
[46] Z. Lu, L. Yang, Y. Guo, *J. Power Sources* **2006**, *156*, 555.
[47] M. Dimitrievska, S. Giraldo, P. Pistor, E. Saucedo, A. Pérez-Rodríguez, V. Izquierdo-Roca, *Sol Energy Mater Sol Cells Cells* **2016**, *157*, 462.
[48] C. Niu, Y. Gong, R. Qiu, Q. Zhu, Y. Zhou, S. Hao, W. Yan, W. Huang, H. Xin, *J. Mater. Chem. A* **2021**, *9*, 12981.